Mechanical Activation Enhanced Solid-State Synthesis of NaCrO$_2$ Cathode Material

Mei Luo,[a] Angel L. Ortiz,[b] Fangmin Guo,[c] Zhepu Shi,[a] Ling Li,[a] Yang Ren,[c] Xiaoyi Zhang,[c] Zonghai Chen,[c] Leon L. Shaw [a,*], Wei Chen[a]

[a] Department of Mechanical, Materials and Aerospace Engineering,
Illinois Institute of Technology, Chicago, IL 60616, USA
[b] Departamento de Ingeniería Mecánica, Energética y de los Materiales,
Universidad de Extremadura, Badajoz, 06006, Spain
[c] Argonne National Laboratory, Argonne, IL 60439, USA

Abstract

NaCrO$_2$ has been studied lately as a promising cathode material for Na-ion batteries. Consequently, we have conducted the first investigation on how high-energy ball milling before the high temperature reaction influences the synthesis reaction of NaCrO$_2$ derived from the typical Na$_2$CO$_3$ and Cr$_2$O$_3$ reactants. In-situ synchrotron X-ray diffractometry is employed for the first time to provide a comprehensive understanding of the critical reaction temperatures and reaction pathway. It is found that high-energy ball milling at room temperature can result in significant changes in the synthesis reaction of NaCrO$_2$ when compared to reactants without high-energy ball milling. These changes include a decreased onset temperature for the formation of O3-NaCrO$_2$, an increased reaction kinetics, an alternation of the reaction pathway, and a complete reaction at 900 °C to form thermally-stable O3-NaCrO$_2$ phase. These phenomena have been ascribed to the mechanical activation induced by high-energy ball milling before high temperature reaction. In contrast, without high-energy ball milling the reaction product at 900 °C is a highly impure NaCrO$_2$ with a poor thermal stability. The thermally-stable O3-NaCrO$_2$ powder produced with mechanical activation of the reactants at RT has much higher specific capacity (~115 mAh/g) than the Na-deficient NaCrO$_2$ powder with unreacted Cr$_2$O$_3$ generated without mechanical activation of the reactants at RT. Furthermore, the thermally-stable O3-NaCrO$_2$ powder exhibits the best capacity retention among all the NaCrO$_2$ without coatings reported so far in the literature.
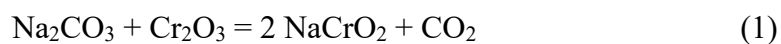
* Corresponding author: lshaw2@iit.edu

I. Introduction

Growing energy and climate concerns are the motivation behind the insatiable interest in the development of new systems of electrical energy storage in general, and in the production of a new generation of rechargeable Na-ion batteries in particular [1-14]. Na is abundant, cheap and safe, and thus offers a viable tantalizing alternative to the rare and costly Li. Furthermore, the chemical properties of Na and Li are similar, which should facilitate the expected transition from the state-of-the-art Li-ion batteries into the future Na-ion batteries. Not surprisingly, intercalation and deintercalation of Na in different layered compounds has been the subject of active research lately, with NaCrO$_2$ emerging as one of the promising cathode materials for use in Na-ion batteries [1,2,10-14]. An important advantage of NaCrO$_2$–based batteries is its high thermal stability, being a safe electrode material because it is more stable than LiCoO$_2$ and LiFePO$_4$ [12]. NaCrO$_2$ is stable in argon up to 1200 °C, but gets oxidized at ~350 °C in oxygen [15]. Accelerating calorimetry experiments reveal that NaCrO$_2$ does not exhibit exothermic reactions until 250 °C, with very little release of heat [12], when in contact with the ethylene carbonate/diethyl carbonate (EC/DEC) solvent in batteries. Furthermore, thermogravimetric analysis (TGA) shows very small mass change due to very little oxygen release. It has been determined that Na$_{0.5}$CrO$_2$ reacts with the EC/DEC solvent transforming into NaCrO$_2$ and P3-CrO$_{2-\delta}$, which gives minimal oxygen release and accounts for the high thermal stability of this cathode material [12].

NaCrO$_2$ is isostructural to LiCrO$_2$ (i.e., both have a rhombohedral (R$\overline{3}$m) O3 type layered structure), but it exhibits different behavior electrochemically. NaCrO$_2$ is able to reversibly deintercalate 0.5 mole of Na ions per formula unit to form Na$_{0.5}$CrO$_2$, thereby providing a theoretical capacity of 125 mAh/g [2]. However, if deintercalation is conducted beyond 0.5 mole of sodium ions per formula unit, one can obtain a charge capacity of ~235

mAh/g, but the discharge capacity is only 90 mAh/g, i.e., irreversible capacity loss occurs [13]. This irreversible capacity loss has been identified to be related to the irreversible migration of Cr ions from the octahedral sites in CrO_2 slabs to both tetrahedral and octahedral sites in the interslab layer [14]. Note that structural change also takes place even for deintercalation of 0.5 mole of Na ions per formula unit from $NaCrO_2$ to $Na_{0.5}CrO_2$, leading to the phase transitions of rhombohedral O3 → monoclinic O3 → monoclinic P3 for the charge process [1]. However, the structural change for Na deintercalation within 0.5 mole of Na ions per formula unit is reversible because Cr ions remain at the octahedral sites in CrO_2 slabs [1]. This is quite different from Li deintercalation in $LiCrO_2$, during which irreversible migration of Cr(VI) from the octahedral sites into the tetrahedral sites takes place owing to disproportionate transfer of Cr(IV) to Cr(III) and Cr(VI) [2]. Little or no irreversible migration of Cr ions into the tetrahedral sites when deintercalation within 0.5 mole of Na ions per $NaCrO_2$ is attributed to the mismatch between $Cr^{VI}O_4^{2-}$ and the O-O bond length and the CrO_2 slab distance of the interstitial tetrahedron [2]. Magnetic measurement has confirmed that chemically deintercalated $Na_{1-x}CrO_2$ contains Cr(IV) [2,13]. A separate study [15] using in-situ and ex-situ X-ray and electron diffraction has revealed a slightly different composition for the onset of the layered-to-rock-salt transformation. It is shown that Na_xCrO_2 $(0 < x < 1)$ remains in the layered structure without Cr migration up to a composition of $Na_{0.4}CrO_2$ [15]. Further removal of Na beyond this composition triggers a layered-to-rock-salt transformation, which results in cycle instability of $NaCrO_2$ [15].

$NaCrO_2$ is typically synthesized through the reaction between Na_2CO_3 and Cr_2O_3 powders at 900 °C [2,11-14] for various hours, which is generally described via the following equation [16]

$$Na_2CO_3 + Cr_2O_3 = 2\ NaCrO_2 + CO_2 \tag{1}$$

Very recently, some of us found that the defect structure in the $NaCrO_2$ crystals so produced can be altered if the reactant mixture is subjected to high-energy ball milling at room temperature (RT) before the high temperature reaction [17]. Furthermore, the electrochemical behavior of these $NaCrO_2$ crystals was found to be influenced by their structural defects [17]. Specifically, the $NaCrO_2$ crystals resulting from the simple mixture of reactants without high-energy ball milling exhibit gradual decay in the specific capacity over charge/discharge cycles,

3

whereas the $NaCrO_2$ crystals derived from the reactant mixture subjected to high-energy ball milling at RT before the high temperature reaction exhibit excellent specific capacity retention and high Coulombic efficiency during electrochemical charge/discharge cycles [17].

Stimulated by the aforementioned interesting results, we have designed and conducted the first study of how high-energy ball milling at RT affects the subsequent synthesis reaction of $NaCrO_2$ crystals derived from Na_2CO_3 and Cr_2O_3 reactants. In order to provide a comprehensive understanding of the critical reaction temperatures and reaction pathway, in-situ synchrotron X-ray diffractometry (SXRD) has been utilized in this study. The findings obtained from in-situ SXRD are then corroborated through TGA, scanning electron microscopy (SEM) and energy-dispersive spectrometry (EDS). We will show that the mechanical activation induced by high-energy ball milling at RT reduces the reaction temperature and alters the reaction pathway for the formation of $NaCrO_2$, thus leading to higher-quality $NaCrO_2$ powders. The details of experimental procedures and the major findings are described in the next several sections.

II. Materials and Methods

2.1 Material Synthesis

The two starting materials, Na_2CO_3 and Cr_2O_3, were procured from Sigma-Aldrich (St. Louis, MO, USA). To identify the effect of mechanical activation, Na_2CO_3 and Cr_2O_3 powders were first mixed in a 1:1 molar ratio using a mortar and pestle. Next, the powder mixture was subjected to high-energy ball milling at RT for 10 h under an Ar atmosphere using an 8000M SPEX Mill with a 10:1 ball-to-powder charge ratio. Stainless steel balls of 6.4 mm in diameter and a stainless container were utilized for ball milling. To avoid overheating, ball milling was stopped for 10 min after each 1-h ball milling, which limited the canister temperature to below 60 ºC. At the completion of ball milling the powder was taken out from the milling container in an Ar-filled glovebox, and then loaded and sealed in an Ar-filled bottle for later use.

2.2 In-Situ Synchrotron X-ray Diffractometry (SXRD)

For the in-situ SXRD experiment the ball milled powder was pressed into a thin pellet, which was then loaded into a custom-made heating chamber. A flowing Ar gas was turned on

immediately after sample loading. Pellet pressing and sample loading into the heating chamber were conducted in ambient air, and lasted about 10 min.

The in-situ SXRD experiments were carried out at the beamline 11-ID-D at the Advance Photon Source (Argonne National Laboratory). The pressed pellet sample was loaded in the center of the sample holder, which was fixed into a Linkam TS1500 high-temperature furnace perpendicular to the incoming X-ray beam. The beam energy was 16 keV, corresponding to a wavelength of 0.774901 Å, and the beam radiation area was 0.2×0.4 mm². The in-situ experiment was performed from RT to 900 °C with a heating rate of 5 °C/min, and then held at 900 °C for 2 h. The entire heating and holding processes were done under a flowing Ar atmosphere. The diffraction Debye patterns were collected using a Pilatus detector with 172×172 μm² pixel size, ~280 mm away from the sample. Exposure time was 10 seconds per SXRD pattern. A standard CeO_2 powder (NIST Standard Reference Material SRM-674a) was used to calibrate the sample-detector distance and other relevant parameters, such as the accurate beam center and detector tilt.

For the sake of comparison, the as-received Na_2CO_3 and Cr_2O_3 powders were also mixed using a mortar and pestle in a 1:1 molar ratio. After uniform mixing, the resulting powder mixture was pressed into a thin pellet directly without high-energy ball milling. This sample is denoted as "no ball milling" (No-BM) hereafter. In contrast, the sample subjected to 10-h high-energy ball milling described above is termed as "ball-milled 10h" (BM-10h). No-BM sample was also investigated using in-situ SXRD under identical conditions as BM-10h sample.

For analysis of SXRD patterns, pattern refinement was conducted when needed. Specifically, lattice parameters were calculated by Pawley refinement of the SXRD patterns, which fits the patterns without reference to the whole crystal structures of the phases present but only using their space group and dimensions of the unit cells and treating the intensities as free parameters.

2.3 Material Characterization

In addition to the in-situ SXRD experiments, No-BM and BM-10h samples were also individually pressed to form pellets, and heated to 900 °C in a tube furnace under a flowing Ar atmosphere. The heating rate was 5 °C/min, similar to that used in the in-situ SXRD

experiments. After reaching 900 $^\circ$C the samples were cooled down immediately, and then analyzed using SEM equipped with EDS to determine their particle sizes, morphologies, and average chemical composition. The Oxford INCA software was used for EDS data acquisition and analysis. To obtain the reliable average composition of each powder sample, EDS spectra were collected in at least 10 different areas. Pure copper was used for EDS calibration before the measurement started. Once calibrated, identification of all elements and their quantities were derived from the internal standards provided in the INCA software.

TGA was also performed for pure Na_2CO_3, pure Cr_2O_3, and pressed $Na_2CO_3+Cr_2O_3$ pellets with and without 10h high-energy ball milling. TGA was always conducted with a heating rate of 5 $^\circ$C/min from RT to 900 $^\circ$C under a flowing Ar atmosphere. This set of experiments provided weight loss information from which one can deduce the onset temperatures for thermal decomposition of pure compounds and for the reaction between un-milled and ball milled $Na_2CO_3+Cr_2O_3$ mixtures during the heating process from RT to 900 $^\circ$C without holding. Thus, the data obtained from TGA, SEM, EDS and in-situ SXRD can be compared directly for the heating process from RT to 900 $^\circ$C without holding.

2.4 Electrochemical Evaluation

Both BM-10h and No-BM powders after subjecting to the 900 $^\circ$C reaction for 2 h were then used to fabricate half cells to evaluate their electrochemical performance. The half cells were made with a Na disc as the counter electrode with the aid of a CR2032 coin cell machine (MTI Corp., Richmond, CA). The working electrode was prepared using a slurry by mixing the $NaCrO_2$ powder, carbon black (CB) and polyvinylidene fluoride (PVDF) in a 60:30:10 weight ratio with N-methyl-pyrrolidone (NMP) as the solvent. The uniform slurry was cast onto an aluminum foil current collector and dried in a vacuum oven at 60 °C for 6 hours and then at 120 °C for additional 6 hours. The half cells were fabricated in an argon-filled glovebox (H_2O <10 ppm and O_2 <1 ppm). The $NaCrO_2$ loading in each cathode was ~0.94 mg/cm^2 and the electrolyte used was 1.0M $NaPF_6$ in propylene carbonate (PC) with addition of 2 vol.% of fluoroethelyene carbonate (FEC). Charge/discharge of all coin cells were conducted at a C rate of 0.25 with respect to the weight of the active material (1C = 125 mA/g $NaCrO_2$) using multiple Neware BTS3000 Battery Testers between 2.0 and 3.6 V vs. Na/Na$^+$.

III. Results and Discussion

3.1 In-Situ SXRD

Figure 1 shows the three-dimensional plot of the 578 SXRD patterns collected *in situ* while heating No-BM sample. The first 332 SXRD patterns were measured during the non-isothermal heating regime from 30 to 900 °C, while the remaining 246 SXRD patterns were acquired during the isothermal heating regime at 900 °C as a function of holding time from 0 to 120 min. Clearly, it can be observed in Figure 1 that there are diffraction peaks appearing and disappearing, as well as simple and complex peak-shifting phenomena, thus indicating the eventual occurrence of structural/crystallographic changes (i.e., possible unit-cell modifications, phase transformations, and reactions).

To properly identify the different events occurring during the non-isothermal and isothermal heating regimes, Figure 2 shows the two-dimensional contour plot generated from the SXRD patterns in Figure 1. In Figure 2 (and later Figure 6), the temperature scale (30 °C to 900 °C) is divided into 10 steps. Similarly, the time scale during holding at 900 °C (0 to 120 min) is divided into 10 steps as well. Furthermore, several horizontal lines are added to highlight the occurrence of the major phase transformations and reactions to be discussed below. In addition, to facilitate the observation by readers, SXRD patterns of the starting materials with and without 10-h ball milling were re-plotted in Figure S1 (Supplementary Materials) where their SXRD patterns are compared with the standards of Cr_2O_3 (JCPDS #: 00-038-1479) and Na_2CO_3 (JCPDS #: 00-037-0451) directly. Moreover, SXRD patterns of the final products of BM-10h and No-BM samples after holding at 900 °C for 2 h are compared with the standard of $NaCrO_2$ (JCPDS #: 00-025-0819) in Figure S2 (Supplementary Materials).

There are multiple interesting features in Figures 2, S1 and S2, as discussed below. First, at RT (i.e., 30 °C) No-BM sample contains both Cr_2O_3 (trigonal, space group $R\bar{3}c$) and γ-Na_2CO_3 (monoclinic, space group $C2/m$). This is inferred from the presence, for example, of the strong 012, 104, 110, and 113 diffraction peaks at ~12.27, 16.75, 18.1, and 20.54° 2θ, respectively, for Cr_2O_3, and of the weaker 112, 202, $\bar{2}$03, and $\bar{2}$22+$\bar{1}$13 diffraction peaks at ~18.85, 19.75, 22.94, and 23.75° 2θ, respectively, for γ-Na_2CO_3. With increasing temperature, the diffraction peaks of both Cr_2O_3 and γ-Na_2CO_3 shift gradually towards lower diffraction

angles, which reflects the expected thermal expansion of the unit cell of these two compounds. The temperature dependence of the cell parameters is linear for Cr_2O_3, but it has a complex behaviour for γ-Na_2CO_3 because the thermal expansion is anisotropic being larger for its lattice parameter c.

Second, at ~350 °C γ-Na_2CO_3 transforms into β-Na_2CO_3 (monoclinic, space group $C2/m$). The thermal expansion of β-Na_2CO_3 is even more anisotropic than that of γ-Na_2CO_3, with its lattice parameters a and c increasing but b and β decreasing, thus resulting in a complex temperature dependence. Indeed, the lattice parameters a and b gradually converge into the same value, while the lattice parameter β decreases progressively towards 90°. In other words, with increasing temperature the (intermediate-temperature) Na_2CO_3 monoclinic structure evolves towards a (high-temperature) Na_2CO_3 hexagonal structure. Furthermore, at ~500 °C β-Na_2CO_3 transforms into α-Na_2CO_3 (hexagonal, space group $P6_3/mmc$). The temperature dependence of the cell parameters is linear for α-Na_2CO_3, similar to the case of Cr_2O_3.

Third, at ~640 °C Cr_2O_3 and α-Na_2CO_3 start to react together forming O3-$NaCrO_2$ (trigonal, space group $R\bar{3}m$), as inferred from the presence, for example, of the 107, 110, 1010, and 0012 diffraction peaks at ~26.06, 30.11, 32.97, and 33.60° 2θ. Also note for example that the absence of diffraction peaks at the near-left side of the 006 diffraction peak and at the near-right side of the 012 and 104 diffraction peaks rules out the formation of both O'3-$NaCrO_2$ (monoclinic, space group $C2/m$) and P'3-$NaCrO_2$ (monoclinic, space group $C2/m$), while the very low intensity of the 015 diffraction peak at ~22.16° 2θ rules out the formation of P3-$NaCrO_2$ (trigonal, space group $R3m$). By way of example, Figure 3 shows a selection of SXRD patterns validating these general observations. With increasing temperature up to 900 °C, the diffraction peaks of O3-$NaCrO_2$ also shift gradually towards lower diffraction angles, thus indicating that thermal expansion dominates the lattice parameters. This effect is also evident in the selection of SXRD patterns shown in Figure 3.

Fourth, intense diffraction peaks of Cr_2O_3 are detected throughout the entire in-situ study in both non-isothermal (30–900 °C) and isothermal (0–120 min at 900 °C) regimes. This finding is also evident in the selection of SXRD patterns shown in Figure 3. The presence of a substantial amount of unreacted Cr_2O_3 indicates an incomplete solid-state synthesis reaction. Given that the starting No-BM sample contained nominally Cr_2O_3 and Na_2CO_3 in a

stoichiometric ratio, the Cr_2O_3 excess in the reaction product would thus suggest the loss of the Na source during the synthesis. When O3-$NaCrO_2$ is formed, the diffraction peaks of Cr_2O_3 become (apart from less intense) markedly sharper, thus suggesting that the smaller Cr_2O_3 crystallites have reacted to form $NaCrO_2$ while the larger ones have not or reacted much slower.

Fifth, during the isothermal heating regime at 900 °C the diffraction peaks of Cr_2O_3 remain in place, which is indeed the expected trend under isothermal heating. However, the diffraction peaks of O3-$NaCrO_2$ shift gradually towards higher diffraction angles. Also importantly, with increasing holding time at 900 °C the intensity of the diffraction peaks of Cr_2O_3 increases, while on the contrary the intensity of the diffraction peaks of O3-$NaCrO_2$ decreases. For example, the ratio of the integrated intensities of the 116 peak of Cr_2O_3 to the 107 peak of O3-$NaCrO_2$ is ~2.7, 3.2, and 4.2 at the beginning (0 min), middle (60 min), and ending (120 min) of the isothermal heating at 900 °C, respectively. These two observations are also evident in the selection of SXRD patterns shown in Figure 3. The peak shifting towards higher diffraction angle is a surprise because it reflects the gradual reduction of the lattice parameters of O3-$NaCrO_2$ during the isothermal heating at 900 °C. It is hard to infer if the same effect occurs or not during the non-isothermal heating because the thermal expansion of the unit cell dominates the lattice parameters. As shown in Figure 4, the measurement of the lattice parameters during the isothermal heating (determined by the Pawley fitting of SXRD patterns, an example of which is shown in Figure S3 in Supplementary Materials) confirms the progressive reduction of the unit cell dimension of O3-$NaCrO_2$ with decreases in both lattice parameters a and c. The reduction is, however, markedly greater for the lattice parameter c (~0.135 Å, or ~0.832%) in relation to the lattice parameter a (~0.01 Å, or 0.333%). The gradual decrease and increase of the diffraction peaks of Cr_2O_3 and O3-$NaCrO_2$, respectively, is a surprise too because it implies that $NaCrO_2$ transforms into Cr_2O_3. It is important to note that the unexpected transformation from O3-$NaCrO_2$ to Cr_2O_3 is not accompanied by appearance of Na_2O, which rules out the occurrence of the decomposition reaction of $2NaCrO_2 \rightarrow Cr_2O_3 + Na_2O$. The likely explanation for the simultaneous occurrence of peak shifting and peak intensity modification is then as follows. According to an earlier study [17], the O3-$NaCrO_2$ obtained by solid-state reaction of the Cr_2O_3 and Na_2CO_3 reactants without prior high-energy ball milling at RT would have a crystal structure with a high concentration of different point

defects (i.e., Na and O vacancies, as well as misplacement of Cr at Na sites). This would also be the present scenario because the synthesized $NaCrO_2$ product has Na deficiency. This highly-defective $NaCrO_2$ crystals would have a poor thermal stability at high temperatures, and would then evolve gradually towards a less-defective Na-richer $NaCrO_2$ crystals along with the precipitation of Cr_2O_3.[1] This explanation accounts for all the experimental observations, as discussed below. The Na-richer chemical composition entails a decrease in the lattice parameters of O3-$NaCrO_2$, and therefore explains the peak shifting towards higher diffraction angles. Note that the O3-$NaCrO_2$ lattice is made up of slabs of edge-sharing CrO_6 octahedra, with Na^{1+} ions octahedrally coordinated between adjacent CrO_6 sheets. Thus, with increasing Na content in the structure, the lattice parameter c decreases due to the lower repulsion between the CrO_2 layers and greater attraction between the Na layer and the adjacent CrO_2 layers. In a lesser extent, the lattice parameter a decreases as well due to the contraction of the CrO_6 octahedra as point defects are annealed out. In addition, the concomitant precipitation of Cr_2O_3 would explain both the intensity increase of the Cr_2O_3 peaks and the intensity decrease of the $NaCrO_2$ peaks. Whichever the case is, the undisputable fact is that No-BM sample led to a highly impure $NaCrO_2$ powder with a poor thermal stability.

Figure 5 shows the three-dimensional plot of the corresponding 578 SXRD patterns collected *in situ* during the non-isothermal (30–900 °C) and isothermal (0–120 min at 900 °C) heating of BM-10h sample, whereas Figure 6 shows the two-dimensional contour plot generated from these SXRD patterns. Again, there are also appearance and disappearance of diffraction peaks, as well as peak-shifting phenomena. However, there are several marked distinctions in comparison with No-BM sample, as discussed below.

First, at room temperature BM-10h sample has a similar SXRD pattern as No-BM sample (Figure S1), i.e., contains both Cr_2O_3 and γ-Na_2CO_3, with the former dominating the
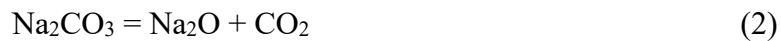
---

[1] The evolution for a highly-defective $NaCrO_2$ crystal structure with a concentration x of Na^{1+} vacancies, a concentration y of Cr^{3+} misplacement at Na^{1+} sites, and a concentration δ of O^{2-} vacancies (where $\delta = \frac{1-x-3y}{2}$ to ensure charge neutrality) would be described by:

$$Na_x Cr_y CrO_{\frac{3+x+3y}{2}} \rightarrow \frac{x}{z} Na_z Cr_j CrO_{\frac{3+z+3j}{2}} + \frac{z+zy-x-xj}{2z} Cr_2O_3$$

where $0 \leq x \leq 1$, $0 \leq y \leq \frac{1-x}{3}$, $0 \leq z \leq 1$, $x < z$, and $y > j$.

SXRD pattern. However, the SXRD pattern of BM-10h sample exhibits peak broadening relative to that of No-BM sample because 10-h ball milling has refined the crystallite sizes to the nanoscale and likely introduced a large number of structural defects to crystalline compounds [18-20]. Refining crystallite sizes to the nanoscale also leads to weaker peak intensity [18-20]. This phenomenon in conjunction with the low scattering factors of Na, C and O in relation to Cr has made several Na_2CO_3 peaks less visible, but still identifiable in Figure S1. Equally important, it should be noted that diffraction peaks of any other compounds (except Cr_2O_3 and Na_2CO_3) are not observed from BM-10h sample (Figure S1), suggesting that Cr_2O_3 and γ-Na_2CO_3 did not react during high-energy ball milling at RT. These phenomena are consistent with the expectation because the Gibbs free energy change for reaction (1) is positive (i.e., 35,124 J/mol $NaCrO_2$) at RT [21]. Because of such a large energy barrier for reaction (1) at RT, $NaCrO_2$ is not expected to form in situ during high-energy ball milling. As shown in Figure S4, the Gibbs free energy change for reaction (1) will not be negative until temperature is higher than 475 °C. In addition, it is known that the local temperature at the collision site during high-energy ball milling is 200 °C – 250 °C higher than the average ball milling temperature (< 60 °C) of the canister [22,23]. This temperature spike at the collision site is in a very short duration (of the order of 10^{-6} – 10^{-5} s) [22,23]. Even with this temperature spike the temperature at the collision site (< 310 °C) is still much lower than that (475 °C) required for the Gibbs free energy change to be negative. Thus, no $NaCrO_2$ is expected to form during high-energy ball milling even with the consideration of the local temperature spike at the collision site.

In addition, Na_2CO_3 is not expected to decompose during high-energy ball milling either because the Gibbs free energy change for reaction (2) is 275,367 J/mol Na_2O at RT [21].

$$Na_2CO_3 = Na_2O + CO_2 \qquad\qquad\qquad (2)$$

In addition, high-energy ball milling at RT cannot lead to mixing of Na_2CO_3 and Cr_2O_3 reactants at the atomic level (e.g., Na-Cr bond formation) because the enthalpy change of reaction (1) is very positive at RT (58,950 J/mol $NaCrO_2$). This reasoning is based on earlier studies [18,24] which used nuclear magnetic resonance spectroscopy to unambiguously establish that reactants can only be mixed very intimately if the enthalpy change of reaction is

positive. Thus, high-energy ball milling at RT has resulted in intimate mixing of Na_2CO_3 and Cr_2O_3 with nano-sized crystallites, high structural defects, and large specific surface area all of which lead to mechanical activation, i.e., increase the enthalpy of the reactants and can greatly accelerate reactions in the subsequent high temperature treatment.

The second important phenomenon from the in-situ SXRD patterns of BM-10h sample is that the thermal expansion of the unit cell is linear for Cr_2O_3 and non-linear for γ-Na_2CO_3, and, again, that the $\gamma \rightarrow \beta$ and $\beta \rightarrow \alpha$ transformations of Na_2CO_3 are observed. In addition, diffraction peaks of Fe (wear debris from the balls and container) are not observed in these SXRD patterns, suggesting that wear debris, if present, is below the detection limit of SXRD or Fe impurity has been dissolved in $O3$-$NaCrO_2$ and Na-deficient $P2$-$NaCrO_2$ as substitutional solutes (i.e., Fe at Cr site).

Third, the formation of $O3$-$NaCrO_2$ takes place at ~600 °C, i.e., 40 °C lower than No-BM sample. Together with the formation of $O3$-$NaCrO_2$ there also appears a transient intermediate compound, which is identified to be Na-deficient $P2$-$NaCrO_2$ (hexagonal, space group $P6_3/mmc$) according, for example, to the 004, 100, 102, 103, 104, and 110 diffraction peaks at ~16.37, 17.19, 19.05, 21.14, 23.81, and 30.21° 2θ. To facilitate the observation by readers, SXRD patterns of BM-10h sample at 675 °C and 900 °C are re-plotted in Figure 7 where they are also compared with the standards of $NaCrO_2$ (JCPDS #: 00-025-0819) and Na-deficient $P2$-$NaCrO_2$ (calculated theoretically). As shown in Figure 7, both $P2$-$NaCrO_2$ and $O3$-$NaCrO_2$ phases are co-present at 675 °C. However, $P2$-$NaCrO_2$ phase has disappeared completely at 900 °C, indicating that Na-deficient $P2$-$NaCrO_2$ has gradually transformed to $O3$-$NaCrO_2$ phase between 675 and 900 °C. Recall that $P2$-$NaCrO_2$ is not observed for No-BM sample, indicating that high-energy ball milling at RT has altered the reaction pathway in forming $NaCrO_2$.

Fourth, a close examination of Figure 6 reveals that Na-deficient $P2$-$NaCrO_2$ disappears at ~750 °C (~150 °C after its formation), and its disappearance is not accompanied with appearance of additional diffraction peaks. This suggests that the greater sodiation of Na-deficient $P2$-$NaCrO_2$ has led to the formation of additional $O3$-$NaCrO_2$. Furthermore, the reactants are completely consumed at ~750 °C in forming $O3$-$NaCrO_2$ without leaving residuals in the final powder. However, detailed analysis of the SXRD patterns has revealed

reduced diffuse scattering at ~825 °C (as evidenced by the lower intensity background), suggesting that synthesis reaction could still have proceeded with amorphous or tiny crystallites in the range ~750–825 °C. Whichever the case is, it is clear that high-energy ball milling has led to the formation of high-purity O3-NaCrO$_2$ powders in the heating process from RT to 900 °C with a heating rate of 5 °C/min.

Fifth, during the isothermal holding regime at 900 °C the diffraction peaks of O3-NaCrO$_2$ remain essentially in place and there is no precipitation of other compounds. Indeed, as shown in Figure 4, in this case the measurement of the lattice parameters during the isothermal holding indicates a minimal reduction of the lattice parameter a (~0.003 Å, or 0.114%) and minimal increase of the lattice parameter c (~0.019 Å, or 0.115%). Consequently, high-energy ball milling has led to an O3-NaCrO$_2$ product with great thermal stability at high temperature.

It is therefore clear that the ball-milled reactants exhibit several distinct features in comparison to the simply-mixed reactants, namely, (*i*) a decreased onset temperature for the reaction to form O3-NaCrO$_2$, (*ii*) an increased reaction kinetics, (*iii*) an alternation of the reaction pathway with the formation of metastable Na-deficient P2-NaCrO$_2$ which transforms to stable O3-NaCrO$_2$ phase in a 150 °C temperature range, and (*iv*) a complete reaction between reactants at 900 °C (even at temperatures close to 750-825 °C if high-energy ball-milling lasts as long as 10 h) to form thermally-stable O3-NaCrO$_2$ phase. In sharp contrast, No-BM sample has led to a highly impure NaCrO$_2$ powder with a poor thermal stability (Figure 4 and Figure S2).

These phenomena can be rationalized as follows. It is known that intensive high-energy ball milling at RT can generate nanostructured particles, introduce structural defects to reactants, and create large surface area all of which increase the enthalpy of the reactants and thus the reaction driving force to form new compounds [25,26]. Because of this increased reaction driving force, metastable phases like Na-deficient P2-NaCrO$_2$ can be formed. Because of the reduction in the reactant particle size and the increase in their surface area and thus the reaction interface, reaction kinetics can be increased substantially so that the onset and completion temperatures for reactions are decreased. An earlier study has shown that high-energy ball milling of elemental Si at RT can result in acceleration of Si nitridation at 1250 °C

by a factor of 9 when compared with Si powder without ball milling [19]. Furthermore, it has been demonstrated that the reactants subjected to high-energy ball milling at RT can react to form carbides, nitrides and their composites at temperatures several hundred degrees (200 to 500 $^{\circ}$C) lower than the reactants without high-energy ball milling [20,27-30]. The result obtained here is consistent with the mechanical activation effects demonstrated by these earlier studies [19,20,27-30], i.e., the onset temperature and completion temperature for forming $NaCrO_2$ have been reduced by mechanical activation at RT. However, the present study additionally shows that a new reaction pathway has been created for $NaCrO_2$ formation. Furthermore, the $NaCrO_2$ formed with mechanical activation at RT is a thermally stable phase, whereas the $NaCrO_2$ formed without mechanical activation at RT is a thermally unstable phase.

3.2 Thermogravimetric Analysis

Figure 8 shows TGA curves for both pure Na_2CO_3 and Cr_2O_3 under a flowing Ar atmosphere. It is noted that Na_2CO_3 starts to exhibit weight loss at ~760 $^{\circ}$C, but significant weight loss does not occur until 851 $^{\circ}$C (Figure 8a), the melting point of Na_2CO_3 [31]. This result is in good accordance with an earlier study [32] showing that Na_2CO_3 can gradually decompose to Na_2O and CO_2 in the liquid state as described by Eq. (2). The weight loss for Cr_2O_3 starts at ~690 $^{\circ}$C and becomes discernible easily above 800 $^{\circ}$C (Figure 8b). However, the weight loss quantity is small with the accumulated weight loss up to 900 $^{\circ}$C being only 1.75%.

Figure 9 shows TGA curves of both un-milled and ball milled $Na_2CO_3+Cr_2O_3$ mixtures under a flowing Ar atmosphere. When Na_2CO_3 and Cr_2O_3 are simply mixed together to form a pellet, it is interesting to find that weight loss starts at 540 $^{\circ}$C (Figure 9a), much lower than the onset temperatures of weight loss for both pure Na_2CO_3 (760 $^{\circ}$C) and Cr_2O_3 (690 $^{\circ}$C) individually. Clearly, the substantial decrease in the onset temperature for weight loss is due to the reaction between Na_2CO_3 and Cr_2O_3. According to Eq. (1), the reaction between Na_2CO_3 and Cr_2O_3 leads to the formation of $NaCrO_2$ and CO_2, and the gaseous CO_2 product is responsible for the observed weight loss. It is further noted that although weight loss starts at 540 $^{\circ}$C, the initial weight loss is very small until 720 $^{\circ}$C is reached, suggesting that the reaction kinetics is slow below 720 $^{\circ}$C. Based on Eq. (1), the theoretical weight loss should be 17.0%

(owing to CO_2 evolution) when the reaction between Na_2CO_3 and Cr_2O_3 is 100% completed. Thus, if one takes the observed weight loss as an index to judge the extent of the reaction between Na_2CO_3 and Cr_2O_3, then it can be deduced that in No-BM sample only 3.8% of the reaction takes place from 540 to 720 ^oC and only 86.7% of the reaction is completed when temperature reaches 900 ^oC.

In comparison to No-BM sample, BM-10h sample exhibits a lower onset temperature for weight loss, a much faster reaction kinetics, and a complete reaction between Na_2CO_3 and Cr_2O_3 when temperature reaches 900 ^oC. As shown in Figure 9b, the onset temperature of weight loss for BM-10h sample is 520 ^oC which is 20 ^oC lower than that for No-BM sample. Furthermore, the reaction kinetics is very fast. For example, 3.8% of the reaction is reached at 633 ^oC, about 87 ^oC lower than the corresponding temperature required for No-BM sample (720 ^oC). Moreover, the cumulated weight loss for BM-10h sample is 16.54% when temperature reaches 900 ^oC. This cumulated weight loss is essentially equal to the theoretical weight loss (17.0%) if the reaction between Na_2CO_3 and Cr_2O_3 is 100% completed, suggesting that the reaction between Na_2CO_3 and Cr_2O_3 is practically completed when temperature reaches 900 ^oC in a constant heating rate of 5 ^oC/min.

Note that the TGA results are qualitatively consistent with in-situ SXRD conclusions. First, the complete reaction between Na_2CO_3 and Cr_2O_3 to form $NaCrO_2$ is achieved for BM-10h samples, whereas this is not the case for No-BM samples. Second, BM-10h samples have a lower onset temperature and faster reaction kinetics for the reaction between Na_2CO_3 and Cr_2O_3 than No-BM samples. The onset temperatures for the reaction detected from TGA experiments (520 and 540 ^oC for BM-10h and No-BM samples, respectively) are however lower than those detected from in-situ SXRD experiments (~600 and ~640 ^oC for BM-10h and No-BM samples, respectively). The discrepancy is believed to be due to the sensitivity of SXRD experiments. Taking the weight losses at 600 and 640 ^oC for BM-10h and No-BM samples respectively as the index of the reaction extent between Na_2CO_3 and Cr_2O_3, one can find that the reaction has proceeded by 0.30% and 0.23% for BM-10h sample at 600 ^oC and No-BM sample at 640 ^oC, respectively. These estimations reveal that SXRD under the experimental conditions used in this study can detect the presence of $NaCrO_2$ if the reaction between Na_2CO_3 and Cr_2O_3 has proceeded by ~0.3%. This is a very high sensitivity in

comparison to conventional XRD. There is, however, some discrepancy between SXRD and TGA in the temperature at which the reaction is completed in BM-10 h, which could be due to the combination of various factors such as geometry differences between the two heating chambers used (in SXRD and TGA), exposure times at temperature to collect in-situ SXRD patterns, and intrinsic limitations of SXRD (non-detection of amorphous residues or of residual tiny crystallites as the reactants are consumed, etc.).

3.3 SEM and EDS Analyses

Figure 10 shows SEM images of No-BM and BM-10h samples before and after being heated to 900 ^oC and then cooled down immediately without holding. It is clear that the starting Na_2CO_3 and Cr_2O_3 powders have fine particle sizes (0.3 to ~0.8 μm). With 10h ball milling the particle sizes are further reduced to ~50 to 100 nm (Figure 10c). After being heated to 900 ^oC and then cooled down immediately, both No-BM and BM-10h samples have exhibited growth of particle size. Specifically, No-BM sample has increased the particle size to a range between 0.6 to 1.2 μm (Figure 10b). Furthermore, some particles have displayed flat facets with hexagonal morphology, reflecting the crystal structure symmetry of $NaCrO_2$ (hexagonal O3). BM-10h sample also exhibits particle growth after being heated to 900 ^oC and cooled down immediately, increasing the particle sizes to a range between 80 and 200 nm (Figure 10d). However, most of its particles remain to have round shape with few exhibiting flat facets. The lack of hexagonal morphology is likely due to their small particle sizes.

The fact that BM-10h samples have smaller particles than No-BM samples is in good accordance with the phenomena discovered in both in-situ SXRD and TGA experiments, i.e., BM-10h sample has faster reaction kinetics and lower onset and completion temperatures for $NaCrO_2$ formation than No-BM sample. High-energy ball milling before heating has reduced reactant particle sizes, led to intimate mixing of reactants, and created large interfaces between reactants, thereby greatly enhancing reactions during heating and ending with smaller particles of the reaction product.

To estimate the average composition of the powder product(s), EDS spectra have been collected in at least 10 different areas for both No-BM and BM-10h samples after being heated to 900 ^oC and then cooled down immediately without holding. Note that owing to the use of

EDS area analysis, the EDS data obtained represents the average composition of many particles which are summarized in Table 1. A clear trend can be seen, that is, BM-10h sample contains more Na than No-BM sample. In addition, both BM-10h and No-BM samples have appeared to lose some Cr and Na during heating. These trends can be interpreted as follows. As revealed by the SXRD analyses and TGA data discussed previously, No-BM sample has a higher onset temperature and slower reaction kinetics to form $NaCrO_2$ than BM-10h sample. Furthermore, the reaction between Na_2CO_3 and Cr_2O_3 to form $NaCrO_2$ is not completed when No-BM sample has reached 900 °C (under the heating rate used here). As a result, some Na_2CO_3 has decomposed to Na_2O and CO_2 above the melting temperature of Na_2CO_3 (~851 °C). Since Na_2O is very volatile, it is reasonable to expect that some Na_2O has escaped from the sample, leading to loss of some Na_2O and thus a Na-deficient sample. In contrast, most Na_2CO_3 in BM-10h sample has reacted with Cr_2O_3 because of its fast reaction kinetics (Figure 9b). As a result, most Na is retained in the final product before a large amount of Na_2CO_3 has a chance to decompose and escape as a volatile Na_2O species from BM-10h sample. Loss of some Cr and Na from both BM-10h and No-BM samples can be attributed to loss of some Cr_2O_3 and Na_2CO_3 during heating before their reaction to form $NaCrO_2$ (Figure 8). The key difference is that BM-10h sample has a smaller loss of Na than No-BM sample during heating because of the faster reaction rate of BM-10h sample.

It should be pointed out that the trend identified by the EDS analysis is in agreement with the SXRD analysis which has revealed the loss of the Na source during the in-situ heating process with the presence of unreacted Cr_2O_3 as well as the formation of a Na-deficient and thermally unstable $NaCrO_2$ in the final product of No-BM sample. For BM-10h sample, the SXRD analysis reveals the formation of thermally stable $NaCrO_2$ with no unreacted Cr_2O_3 in the final product, leading to a conclusion that the average Na concentration of BM-10h sample is higher than that of No-BM sample. This conclusion is also consistent with the conclusion derived from the EDS analysis.

3.4 Electrochemical Characterization

Figure 11 presents the typical charge/discharge curves of BM-10h and No-BM half cells at the 1st, 2nd, and 10th cycles, while Figure 12 shows the discharge capacities and coulombic

efficiencies of both half cells as a function of the cycle number. It is noted that the first charge capacity of every cell is always much higher than the first discharge capacity, indicating the presence of irreversible process(es) in the initial charge/discharge cycles. However, the specific capacities of charge and discharge after the first cycle become closer, giving rise to a coulombic efficiency approaching 98% after the second cycle and close to 100% in the subsequent cycles. The phenomenon of low coulombic efficiency at the initial cycles is ascribed to the formation of the solid electrolyte interphase (SEI) layer on the Na anode in the initial cycles [17].

Figure 11 also unambiguously reveals that the specific capacity of BM-10h half cells (~115 mAh/g) is much higher than that of No-BM half cells (~68 mAh/g), demonstrating that the thermally-stable O3-NaCrO$_2$ powder produced with mechanical activation of the reactants at RT has better electrochemical properties than the Na-deficient NaCrO$_2$ powder with unreacted Cr$_2$O$_3$ generated without mechanical activation of the reactants at RT. Furthermore, BM-10h half cells exhibit superior capacity retention over charge/discharge cycles. As shown in Figure 12, the capacity retention of BM-10h half cells is almost 100% over 20 cycles tested in this study. This is the best retention among all the reported NaCrO$_2$ without coatings [2,11,13,17]. Interestingly, No-BM half cells also display good capacity retention in spite of their very low specific capacities (~68 mAh/g). However, the underlying mechanism for this phenomenon is unclear at this stage and will be investigated in future studies.

IV. Concluding Remarks

In-situ SXRD was conducted to investigate the synthesis reaction of NaCrO$_2$ derived from Na$_2$CO$_3$ and Cr$_2$O$_3$ reactants. The findings obtained from in-situ SXRD analyses were corroborated with TGA, SEM and EDS experiments. Based on these experiments and analyses, it is established that high-energy ball milling at RT can lead to significant changes in the synthesis reaction of NaCrO$_2$ when compared to reactants without high-energy ball milling. Specifically, high-energy ball milling at RT has decreased the onset temperature for the formation of O3-NaCrO$_2$, increased the reaction kinetics, altered the reaction pathway with the formation of metastable Na-deficient P2-NaCrO$_2$ phase which transforms to stable O3-NaCrO$_2$ phase in a higher temperature range, and resulted in complete reaction at 900 ºC with the formation of thermally-stable O3-NaCrO$_2$ phase. In contrast, without high-energy ball milling

at RT the reaction product at 900 ºC contains Na-deficient $NaCrO_2$ crystals with a poor thermal stability and unreacted Cr_2O_3. These phenomena have been attributed to the mechanical activation induced by high-energy ball milling at RT, which has led to reduction in particle sizes, intimate mixing of reactants, introduction of high structural defects and large interfacial area. All of these changes brought about by high-energy ball milling can accelerate reactions in the subsequent high temperature treatment and lead to the formation of pure $NaCrO_2$ phase. The thermally-stable $O3$-$NaCrO_2$ powder produced with mechanical activation of the reactants at RT has much higher specific capacity (~115 mAh/g) than the Na-deficient $NaCrO_2$ powder with unreacted Cr_2O_3 generated without mechanical activation of the reactants at RT. Furthermore, the thermally-stable $O3$-$NaCrO_2$ powder exhibits the best capacity retention among all the $NaCrO_2$ without coatings reported so far in the literature.

References:

[1] Y.-N. Zhou, J.-J. Ding, K.-W. Nam, X. Yu, S.-M. Bak, E. Hu, et al., Phase transition behavior of $NaCrO_2$ during sodium extraction studied by synchrotron-based X-ray diffraction and absorption spectroscopy, J. Mater. Chem. A 1 (2013) 11130.

[2] S. Komaba, C. Takei, T. Nakayama, A. Ogata, N. Yabuuchi, Electrochemical intercalation activity of layered $NaCrO_2$ vs. $LiCrO_2$, Electrochem. Commun. 12 (2010) 355–358.

[3] M. Sawicki, L.L. Shaw, Advances and challenges of sodium ion batteries as post lithium ion batteries, RSC Adv. 5 (2015) 53129–53154.

[4] V. Palomares, P. Serras, I. Villaluenga, K.B. Hueso, J. Carretero-González, T. Rojo, Na-ion batteries, recent advances and present challenges to become low cost energy storage systems, Energy Environ. Sci. 5 (2012) 5884–5901.

[5] S.-W. Kim, D.-H. Seo, X. Ma, G. Ceder, K. Kang, Electrode Materials for Rechargeable Sodium-Ion Batteries: Potential Alternatives to Current Lithium-Ion Batteries, Advanced Energy Mater. 2 (2012) 710–721.

[6] M.D. Slater, D. Kim, E. Lee, C.S. Johnson, Sodium-ion batteries, Adv. Funct. Mater., 23 (2013) 947–958.

[7] B.L. Ellis, L.F. Nazar, Sodium and sodium-ion energy storage batteries, Curr. Opin. Solid State Mater. Sci. 16 (2012) 168–177.

[8] H. Pan, Y.-S. Hu, L. Chen, Room-temperature stationary sodium-ion batteries for large-scale electric energy storage, Energy Environ. Sci. 6 (2013) 2338.

[9] S.P. Ong, V.L. Chevrier, G. Hautier, A. Jain, C. Moore, S. Kim, et al., Voltage, stability and diffusion barrier differences between sodium-ion and lithium-ion intercalation materials, Energy Environ. Sci. 4 (2011) 3680–3688.

[10] C.Y. Chen, K. Matsumoto, T. Nohira, R. Hagiwara, A. Fukunaga, S. Sakai, K. Nitta, S. Inazawa, Electrochemical and structural investigation of $NaCrO_2$ as a positive electrode for sodium secondary battery using inorganic ionic liquid NaFSA-KFSA, J. Power Sources, 237 (2013) 52–57.

[11] J.J. Ding, Y.-N. Zhou, Q. Sun, Z.-W. Fu, Cycle performance improvement of $NaCrO_2$ cathode by carbon coating for sodium ion batteries, Electrochem. Commun. 22 (2012) 85–88.

[12] X. Xia, J.R. Dahn, $NaCrO_2$ is a fundamentally safe positive electrode material for sodium-ion batteries with liquid electrolytes, Electrochem. Solid-State Lett. 15 (2012) A1–A4.

[13] S. Komaba, T. Nakayama, A. Ogata, T. Shimizu, C. Takei, S. Takada, A. Hokura, I. Nakai, Electrochemically reversible sodium intercalation of layered $NaNi_{0.5}Mn_{0.5}O_2$ and $NaCrO_2$, ECS Trans. 16 (2009) 43–55.

[14] K. Kubota, I. Ikeuchi, T. Nakayama, C. Takei, N. Yabuuchi, H. Shiiba, M. Nakayama, S. Komaba, New insight into structural evolution in layered $NaCrO_2$ during electrochemical sodium extraction, J. Phys. Chem. 119 (2015) 166-175.

[15] S.-H. Bo, X. Li, A.J. Toumar, G. Ceder, Layered-to-rock-salt transformation in desodiated Na_xCrO_2 (x = 0.4), Mater. Chem. 28 (2016) 1419-1429.

[16] S. Sampath, S.K. Sali, N.C. Jayadevan, Thermochemical studies in the sodium-chromium-oxygen system, Thermochim. Acta 159 (1990) 327-335.

[17] M. Sawicki, A.L. Ortiz, M. Luo, L.L. Shaw, Structural-defect-controlled electrochemical performance of sodium ion batteries with $NaCrO_2$ cathodes, ChemElectroChem. 4 (2017) 3222–3230.

[18] L.L. Shaw, X.-Q. Xie, R.-M. Ren, Z.-G. Yang, NMR studies on mixing of insoluble constituents during high energy milling, Scripta Mater. 39 (1998) 1169–1175.

[19] L.L. Shaw, Z. Yang, R. Ren, Mechanically Enhanced Reactivity of Silicon for the Formation of Silicon Nitride Composites, J. Am. Ceram. Soc. 81 (2005) 760–764.

[20] R.-M. Ren, Z.-G. Yang, L.L. Shaw, Synthesis of Nanostructured TiC via Carbothermic Reduction Enhanced by Mechanical Activation, Scripta Mater. 38 (1998) 735–741.

[21] O. Kubaschewski, C. B. Alcock, and P. J. Spencer, Materials Thermochemistry, 6th Ed., Pergamon Press, Ltd., Headington Hill Hall, Oxford, England, 1993.

[22] R. M. Davis, B. McDermott, C. C. Koch, Mechanical alloying of brittle materials, Metall. Trans. 19A (1988) 2867-2874.

[23] A. K. Bhattacharya, E. Arzt, Temperature rise during mechanical alloying, Scr. Metall. Mater. 27 (1992) 749-754.

[24] X. Xie, Z. Yang, R. Ren, L.L. Shaw, Solid state ^{29}Si magic angle spinning NMR: investigation of bond formation and crystallinity of silicon and graphite powder mixtures during high energy milling, Mater. Sci. Eng. A255 (1998) 39–48.

[25] H. J. Fecht, E. Hellstern, Z. Fu, W. L. Johnson, Nanocrystalline Metals Prepared by High-Energy Ball Milling, Metall. Trans. 21A (1990) 2333-2337.

[26] H. J. Fecht, Synthesis and Properties of Nanocrystalline Metals and Alloys Prepared by Mechanical Attrition, Nanostruct. Mater. 1 (1992) 125-130

[27] R. Ren, Z. Yang, L.L. Shaw, Synthesis of Nanostructured Silicon Carbide through an Integrated Mechanical and Thermal Activation Process, J. Am. Ceram. Soc. 85 (2004) 819–827.

[28] R. Ren, Z. Yang, L.L. Shaw, Synthesis of nanostructured chromium nitrides through mechanical activation process, Nanostructured Mater. 11 (1999) 25–35.

[29] J. Suri, L.L. Shaw, M. F. Zawrah, Synthesis of Carbon-Free Si_3N_4/SiC Nanopowders using Silica Fume, Ceram. Int. 37 (2011) 3477-3487.

[30] Y. Zhong, L.L. Shaw, A study on the synthesis of nanostructured WC-10 wt.% Co particles from WO_3, Co_3O_4 and graphite, J. Mater. Sci. 46 (2011) 6323-6331.

[31] G. J. Janz, E. Neuenschwander, F. J. Kelly, High-temperature heat content and related properties for Li_2CO_3, Na_2CO_3, K_2CO_3 and the ternary eutectic mixture, Trans. Faraday Soc. 59(1963) 841-845.

[32] E. Kocsardy, K. Papp, A. Griger, T. Lakatos, A. B. Kiss, Phase analysis of the red muds by complex thermal infrared and X-ray methods, in Proceedings of the Fifth International Conference on Thermal Analysis, Heyden & Son Ltd., London, Bellmawr, N.J., 1977, pp. 87-90.